Impact of metal adhesion layer diffusion on thermal interface conductance

Dipanjan Saha,[1] Xiaoxiao Yu,[2] Minyoung Jeong,[3] Mohamed Darwish,[4] Jeffrey Weldon,[4] Andrew J. Gellman,[2,5] and Jonathan A. Malen[1,3,*]

[1]*Department of Mechanical Engineering, Carnegie Mellon University, Pittsburgh, Pennsylvania 15213, USA*
[2]*Department of Chemical Engineering, Carnegie Mellon University, Pittsburgh, Pennsylvania 15213, USA*
[3]*Department of Materials Science and Engineering, Carnegie Mellon University, Pittsburgh, Pennsylvania 15213, USA*
[4]*Department of Electrical and Computer Engineering, Carnegie Mellon University, Pittsburgh, Pennsylvania 15213, USA*
[5]*W.E. Scott Institute for Energy Innovation, Carnegie Mellon University, Pittsburgh, Pennsylvania 15213, USA*

(Received 20 July 2018; revised manuscript received 12 December 2018; published 13 March 2019)

Systematic measurements on the impact of interdiffusion between a metal overlayer and adhesion layer on the thermal interface conductance (G) at the metal bilayer-dielectric interface are reported. Composition depth profiles quantify the interdiffusion of a Au-Cu bilayer as a function of Cu adhesion layer thickness (0–10 nm), annealing time, and annealing temperature. Optical pump/probe measurements of G quantify the effect of Au-Cu interdiffusion on thermal transport across the (Au-Cu)-Al_2O_3 interface. The enhancement of G between Au and Al_2O_3 through the addition of a Cu adhesion layer decreases as Au-Cu interdiffusion occurs. For example, annealing a 49-nm Au film with a 4.7-nm Cu adhesion layer on Al_2O_3 at 520 K for 30 min, results in a $57 \pm 15\%$ drop in G. An analytical model of the composition profile is derived with inputs of annealing time, temperature dependent permeabilities of the Au-Cu interface to each species, and the initial thicknesses of the Au and Cu layers. Integrating this model with a diffuse mismatch model defines a methodology for the prediction of G that accounts for interdiffusion in metal bilayers on dielectric substrates, and can be used to evaluate the degradation of G over a device's lifetime.

DOI: 10.1103/PhysRevB.99.115418

I. INTRODUCTION

As increasingly complex electronic device architectures are developed, sufficient heat dissipation becomes ever more challenging. For example, in the field of three-dimensional integration, device stacking leads to a high density of material interfaces, each of which can contribute a significant resistance to heat transfer [1]. In devices where these are metal-semiconductor or metal-dielectric interfaces, thermal transport is primarily a function of phonon transmission because the free electron density is low on the dielectric (or semiconductor) side of the interface [2–4].

Jeong *et al.* showed that the insertion of metal adhesion layers that have a higher phonon density of states overlap with the dielectric than the overlayer metal's overlap, experience significant enhancement of thermal interface conductance (G) between the metal and dielectric [2,5,6]. Adding as little as 1.5 nm of Cu between Au and Al_2O_3 roughly doubles the value of G with respect to that of Au-Al_2O_3. In comparison, Freedman *et al.* showed that at Au_xCu_{1-x}-Al_2O_3 interfaces, the value of G decreases as the Au content, x, increases [7]. While those two works quantify G at the extremes of interdiffusion (no interdiffusion and complete interdiffusion), it is unknown how an intermediate value of interdiffusion would affect G, despite its potential to compromise the thermal benefits of adhesion layers over the lifetime of a device.

*Author to whom correspondence should be addressed: jonmalen@andrew.cmu.edu

While there are pre-existing measurements on the effect of different metal compositions on G [8–10], the outstanding research questions that this work addresses are how temperature treatment affects the interdiffusion of metal bilayer films on dielectric substrates, and how this interdiffusion affects G. Our experiments focus on interdiffusion of the Au-Cu adhesion layer system, and can be compared with several published studies [11–15].

We report x-ray photoelectron spectroscopy (XPS) depth profiles and optical pump/probe measurements of G for Au-Cu thin films of different Cu thicknesses that have been annealed at temperatures in the range 320–520 K for a period of 30 min. These data reveal how annealing temperature and Cu thickness affect the metal bilayer interdiffusion profiles and the subsequent effect on G. An analytical description is derived for the interdiffusion profiles as a function of time, temperature, and initial film thickness in thin Au-Cu bilayer films, and is used as input to a diffuse mismatch model (DMM) in order to predict G.

II. RESULTS AND DISCUSSION

A. Cu and Au film thickness

In order to investigate the effect of adhesion layer thickness on interdiffusion, two samples were prepared in the form of Cu wedges (0–25 nm in thickness) deposited on Mo and Al_2O_3 substrates and then covered with a uniform film of Au (∼44 nm). The thicknesses of the Cu and Au layers were characterized using energy dispersive x-ray (EDX)

 ©2019 American Physical Society

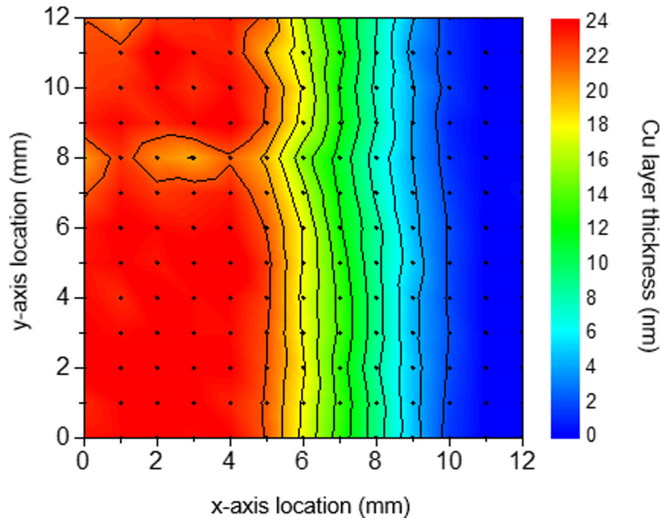

FIG. 1. Color contour map of the Cu adhesion layer thickness across the Au-Cu film on an Al_2O_3 substrate. Thickness was measured using EDX on a 13 × 13 point grid.

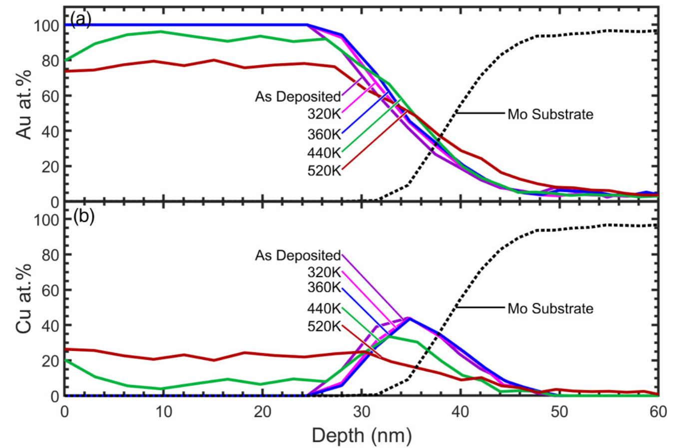

FIG. 2. XPS depth profiles of (a) Au and (b) Cu measured for an 8-nm Cu film with 39 nm of Au deposited on top. The underlying substrate is Mo. The first indication of Cu diffusion across the Au-Cu interface is observed after annealing at 440 K. At this temperature, the Cu is uniformly distributed across the thickness of the Au overlayer. At 520 K, the Au and Cu have fully alloyed. All measurements were conducted on a single sample.

spectroscopy. Figure 1 shows the lateral thickness distribution of the Cu adhesion layer across a 12 × 12 mm^2 area grid with 1 mm spacing, centered on the 14 × 14 mm^2 Al_2O_3 substrate. The maximum thickness of the Cu wedge was 23 ± 1 nm, and decreases linearly to zero across a distance of ∼6 mm. The thickness of the uniform Au layer on top of the Cu wedge was 49 ± 2 nm.

The second sample was prepared on a Mo substrate in order to enable XPS depth profiling to study the interdiffusion between Cu and Au. The EDX map of the Cu film thickness deposited onto the Mo substrate is shown in Fig. S1 (see the Supplemental Material) [16]. The thickness of the Au film on the Mo substrate was 39 ± 1 nm.

B. XPS depth profiles of annealed Au-Cu-Mo interfaces

Depth profiles of the Au-Cu bilayer film on Mo were obtained at various Cu thicknesses and after annealing the sample at temperatures in the range 320–520 K. During depth profiling of multicomponent films, the surface composition measured by XPS can be influenced by the different Ar^+ sputtering rates for the individual alloy components [17–21]. This results in measured surface compositions that differ from the bulk composition [21–23]. During depth profiling of Au-Cu bilayers, the sputtering depth and the bulk composition at each depth can be extracted from the XPS measured surface compositions and the calibrated Ar^+ sputtering rates for each component [24–26].

XPS depth profiles were obtained at four Cu thicknesses (25, 18, 8, and 0 nm) on the Au-Cu-Mo substrate to observe the interdiffusion between Au and Cu as a function of annealing temperature and time. XPS depth profiles measured at a Cu thickness of 8 nm are shown in Fig. 2. Au, Cu, and Mo composition profiles were measured for the as-deposited bilayer and after each 30 min vacuum anneal of the same sample at the temperatures of 320, 360, 440, and 520 K. For the as-deposited film, the interdiffusion between Au and Cu is negligible at room temperature [27,28]. However, the width of the Au-Cu interface observed from the XPS depth profiling appears to be ∼10 nm. This may arise for two reasons: (1) the momentum transfer induced by Ar^+ ion sputtering in the collision cascade region can result in atomic mixing of surface atoms; (2) the nonuniformity of the Ar^+ beam rastering across the 1-mm^2 sputtering area results in nonuniform rates of material removal. Experimental support for (2) can be seen in Fig. 2, which reveals Mo signal at a depth of 35 nm, significantly shallower than the nominal combined metal film thickness of 47 nm. XPS profiles of the bilayer film obtained after heating at temperatures of 320 and 360 K for 30 min were very similar to those obtained from the as-deposited film, indicating negligible interdiffusion of Au and Cu at temperatures ⩽360 K. However, after annealing at 440 K, Cu had crossed the Au-Cu interface, and was uniformly distributed throughout the Au layer to form a Au-Cu alloy with an average of 8 at. % Cu. Subsequent annealing at 520 K for 30 min resulted in Au and Cu becoming completely interdiffused; forming a homogenous alloy with an average composition of 25 at. % Cu.

The uniform distribution of Cu in the Au rich region was also seen in the composition profiles generated by Rutherford backscattering spectrometry, performed by Aleshin *et al.* in their vacuum annealing experiments over the temperature range of 448–523 K [12]. They attributed their profiles to grain boundary diffusion and we hypothesize that the same mechanism is at work in our films.

Interestingly, the XPS data of Fig. 2 shows a buildup of Cu at the surface of the Au film after diffusing through the Au layer during heating at 440 K for 30 min. The same phenomenon was observed in the depth profiles at points on the sample with initial Cu thicknesses of 18 and 25 nm and can also be seen in Fig. S2. This observation is consistent with the experimental results of Aleshin *et al.* [12] and the surface accumulation work of Hwang *et al.* [29].

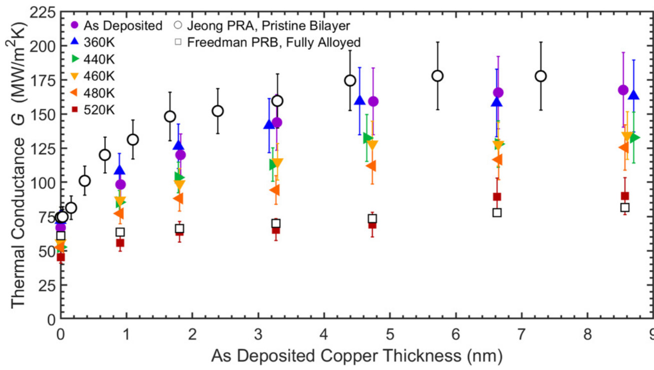

FIG. 3. Measurements of G vs Cu adhesion layer thickness for the films as-deposited, and after subsequent heating to 360, 440, 460, 480, and 520 K for 30 min. The values of G for the as-deposited films are within the error of literature values for pristine films [2]. Values of G after annealing at 360 K are similar to those for the as-deposited film. A significant decrease in G occurs after annealing at 440, 460, and 480 K. At 520 K, G has reached its minimum, in good agreement with the literature values for a fully intermixed alloy [7].

C. Thermal Interface Conductance

Using the laser pump/probe technique, frequency domain thermoreflectance (FDTR), G was measured as a function of adhesion layer thickness and annealing temperature. Measurements of G on the as-deposited film are shown in Fig. 3 and agree within the uncertainty of the measured values reported by Jeong *et al.* [2]. As expected, G rapidly increases as the thickness of the Cu adhesion layer increases from zero, and saturates at higher thicknesses (∼4 nm of Cu). According to the model of Jeong *et al.*, validated for both Cr and Cu adhesion layers, short wavelength phonons from Cu dominate thermal transport across the metal-dielectric interface. As thickness increases in the thin Cu region, longer wavelength phonons that also contribute to G arise within the film. At higher Cu thicknesses, the additional long wavelength phonons have a low density of states and thus contribute little to G causing it to flatten out, as shown in Fig. 3.

After annealing at 360 K, G is similar to that of the as-deposited multilayer films. This is consistent with the depth profiles of Fig. 2, which show that there is negligible interdiffusion of the Au and Cu layers after annealing at 360 K. After annealing at 440, 460, and 480 K, the values of G are notably lower than those obtained from the film annealed at 360 K. While the XPS data of Fig. 2 shows that Cu diffuses into the Au, it is unclear whether Au is diffusing into the Cu region. Au diffusion into Cu is seen more clearly in Fig. S2, where Au increasingly diffuses into the Cu as a function of annealing time. We hypothesize that this diffusion of Au into the Cu region is responsible for lowering G. This hypothesis is founded on the work of Freedman *et al.*, which showed that at Au_xCu_{1-x}-Al_2O_3 interfaces, the value of G decreases as x increases [7]. Further comparison to Freedman's work can be made because Fig. 2 shows that our films are fully intermixed after annealing at 520 K. Using the as-deposited Au and Cu film thicknesses in our samples, the atomic fraction of Au was calculated and the values of G from Freedman's model at these concentrations were used to plot the open squares in Fig. 3. The two sets of data (open squares and solid maroon squares) are in good agreement with one another, further corroborating that complete interdiffusion between Cu and Au has occurred at 520 K.

III. MODELING

In order to extend the use of our experimental data for thermal engineers to predict G for other metal thicknesses and annealing temperatures, a simple composition model with an analytical solution has been developed and integrated with the DMM to predict thermal interface conductance.

A. Interdiffusion Composition Modeling

Classical solutions to Fick's Second Law for diffusion couples and thin films were inappropriate to model our composition profiles because their solutions are complimentary error functions and Gaussians, respectively, which decay to fixed boundary compositions far from the interface [30–33]. In contrast, the nature of diffusion in our thin films leads to uniform concentrations with boundary values that change as a function of annealing conditions. Specifically, Fig. 2 clearly reveals that once the Cu atoms have crossed the Au-Cu interface, they distributed uniformly across the Au layer and Fig. S2 [16] indicates that when Au diffused across the Au-Cu interface, it could also be approximated to have a relatively uniform distribution across the Cu region. Relevant literature [34–41] was unable to represent these regions in our data.

Aleshin *et al.* [12] observed similar profiles, and suggested that diffusion along grain boundaries is the operative mechanism within the films. While Figs. 2 and 3 of Aleshin's work exhibited some uniform composition distributions similar to our data, their Au concentration in Cu decayed to zero and their Cu concentration in the Cu rich region maintained the initial concentration value, whereas ours did not. These differences prevented us from using the Whipple solution [35] to the Fisher model [34] and the Gilmer and Farrell solution for grain boundary diffusion [42,43] as they did. These differences in composition profiles can be attributed to the thicknesses of their films: 200–250 nm of Cu and 45–70 nm of Au (Au diffusion in Cu study), and 800 nm of Cu and 60–120 nm of Au (Cu diffusion in Au study), whereas our Au was ∼44 nm and our Cu thickness ranged from 0–25 nm. For our thicknesses, interactions with free surfaces and substrate interfaces can be important [44]. Our bilayers can be best described as undergoing Type C grain boundary diffusion kinetics (diffusion along the grain boundaries dominate over diffusion from the grain boundary into the adjacent grains) [44,45] between two instantaneous sources (both films are too thin for either to be treated as semi-infinite) [46]. An approximate analytical solution has been described in the work of Hwang *et al.* [29,46–48], but also requires the assumption that the solute spreads along the surface after exiting the solvent, as is common in surface accumulation diffusion measurement techniques, but not observed in our Au diffusion into Cu data. This solution may be appropriate for modeling our data for Cu diffusion into Au, but would require additional details of the dimensions of the grain boundaries and Cu segregation factor at the interface.

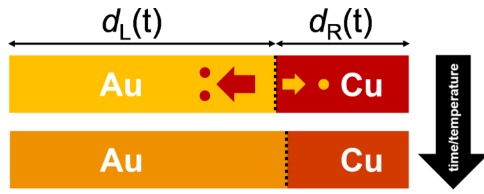

FIG. 4. Depiction of interdiffusion in the metal bilayer where Cu is deposited on a dielectric and capped with Au. According to this schematic, as Cu diffuses to the left and Au to the right, the total thickness is constant but the thickness of each side changes, moving the position of the Au-Cu interface denoted by the black dashed line. The rate at which each species crosses the interface is dependent on the permeability (function of temperature) of the interface to that species, the composition, and time. Once a species crosses the interface, it uniformly distributes itself on that side of the interface.

Seeing that solutions presented in the literature are not well suited to describe our composition data, we derived a simple mass diffusion model in which spatial gradients in composition on either side of the Au-Cu interface are approximated to be zero and therefore, the major resistance to interdiffusion is at the interface itself, as depicted in Fig. 4. This model is only applicable for materials where thicknesses are smaller than diffusion length scales, Type C kinetics are occurring, and the concentration of the uniform composition regions away from the bilayer interface are changing as a function of annealing time/temperature.

The following two equations are generated to describe the net molar flux of Au and Cu, as a function of concentration difference across the interface for each species,

$$\dot{n}_{\mathrm{CuR}}(t) = -P_{\mathrm{Cu}}\left(\frac{n_{\mathrm{CuR}}(t)}{d_{\mathrm{R}}(t)} - \frac{n_{\mathrm{CuL}}(t)}{d_{\mathrm{L}}(t)}\right), \tag{1}$$

and

$$\dot{n}_{\mathrm{AuR}}(t) = P_{\mathrm{Au}}\left(\frac{n_{\mathrm{AuL}}(t)}{d_{\mathrm{L}}(t)} - \frac{n_{\mathrm{AuR}}(t)}{d_{\mathrm{R}}(t)}\right), \tag{2}$$

where n_{Au} and n_{Cu} are the number of moles of Au and Cu per unit area in the plane of the interface, d refers to the thickness, the subscripts L and R designate the side of the interface in accordance with Fig. 4, and P_{Au} and P_{Cu} are interfacial permeabilities to Au and Cu. These permeabilities describe the conductance of the interface to Au and Cu transport. The respective molar fluxes across the interface are equivalent to the molar flux of Cu leaving the right side and the molar flux of Au entering the right side of Fig. 4, respectively.

The system described in Fig. 4 can be thought of as having two containers of different gases separated by an infinitesimally thin membrane, where the membrane has a different permeability to each species. Once a species crosses the interface it will distribute itself uniformly in the new container. The volumes of the containers are allowed to vary with time to capture the effect of the solid films getting thinner/thicker as the net flux across the membrane moves atoms from one side to the other.

As described in the work of Aleshin *et al.* [12], the physical mechanism of mass transport within each film is grain boundary diffusion. Once one species enters the grain boundary of the other, it rapidly diffuses along it. If the Au and Cu films are columnar grained, a possible reason that the dominant mass transport resistance occurs at the interface may be due to a mismatch of grain boundary pathways between the films; an atom easily travels along a grain boundary in each film but needs to travel in-plane in the interfacial region to move from one grain boundary pathway to the other.

In Eqs. (1) and (2) there are six time-dependent unknowns. Two more equations relate the thicknesses to the number of moles of each species,

$$d_{\mathrm{R}}(t) = \frac{N_{\mathrm{A}}a^3}{4}(n_{\mathrm{AuR}}(t) + n_{\mathrm{CuR}}(t)), \tag{3}$$

and

$$d_{\mathrm{L}}(t) = \frac{N_{\mathrm{A}}a^3}{4}(n_{\mathrm{AuL}}(t) + n_{\mathrm{CuL}}(t)), \tag{4}$$

where N_{A} is Avogadro's number and a is the average lattice constant of the conventional cell for a face-centered-cubic crystal structure (this relation is only valid if the two species have similar lattice constants). Substituting Eqs. (3) and (4) into Eqs. (1) and (2) yields

$$\dot{n}_{\mathrm{CuR}}(t) = -\frac{4P_{\mathrm{Cu}}}{N_{\mathrm{A}}a^3}\left(\frac{n_{\mathrm{CuR}}(t)}{n_{\mathrm{AuR}}(t) + n_{\mathrm{CuR}}(t)} - \frac{n_{\mathrm{CuL}}(t)}{n_{\mathrm{AuL}}(t) + n_{\mathrm{CuL}}(t)}\right) \tag{5}$$

and

$$\dot{n}_{\mathrm{AuR}}(t) = \frac{4P_{\mathrm{Au}}}{N_{\mathrm{A}}a^3}\left(\frac{n_{\mathrm{AuL}}(t)}{n_{\mathrm{AuL}}(t) + n_{\mathrm{CuL}}(t)} - \frac{n_{\mathrm{AuR}}(t)}{n_{\mathrm{AuR}}(t) + n_{\mathrm{CuR}}(t)}\right). \tag{6}$$

Mass conservation relations

$$n_{\mathrm{AuL}}(t) = n_{\mathrm{Au}} - n_{\mathrm{AuR}}(t), \tag{7}$$

and

$$n_{\mathrm{CuL}}(t) = n_{\mathrm{Cu}} - n_{\mathrm{CuR}}(t) \tag{8}$$

are substituted into Eqs. (5) and (6) to yield two coupled differential equations, with two unknowns (n_{CuR} and n_{AuR}),

$$\frac{N_{\mathrm{A}}a^3}{4P_{\mathrm{Cu}}}\dot{n}_{\mathrm{CuR}}(t) = \left(-\frac{n_{\mathrm{CuR}}(t)}{n_{\mathrm{AuR}}(t) + n_{\mathrm{CuR}}(t)} + \frac{n_{\mathrm{Cu}} - n_{\mathrm{CuR}}(t)}{n_{\mathrm{Au}} - n_{\mathrm{AuR}}(t) + n_{\mathrm{Cu}} - n_{\mathrm{CuR}}(t)}\right), \tag{9}$$

$$\frac{N_A a^3}{4P_{Au}}\dot{n}_{AuR}(t) = \left(\frac{n_{Au} - n_{AuR}(t)}{n_{Au} - n_{AuR}(t) + n_{Cu} - n_{CuR}(t)} - \frac{n_{AuR}(t)}{n_{AuR}(t) + n_{CuR}(t)}\right). \tag{10}$$

Adding Eqs. (9) and (10) together produces

$$\frac{\dot{n}_{CuR}(t)}{P_{Cu}} + \frac{\dot{n}_{AuR}(t)}{P_{Au}} = 0, \tag{11}$$

which demonstrates that the rates at which Cu and Au cross the interface are proportional to the ratio of their respective permeabilities. Integrating both sides of this equation and substituting in initial conditions $n_{AuR}(0) = 0$, and $n_{CuR}(0) = n_{Cu}$, yields

$$n_{AuR}(t) = \frac{P_{Au}}{P_{Cu}}(n_{Cu} - n_{CuR}(t)), \tag{12}$$

assuming that P_{Au} and P_{Cu} are independent of time. Substituting Eq. (12) into Eq. (9) and (10) results in the following two ordinary differential equations:

$$\dot{n}_{CuR}(t) = \frac{4P_{Cu}}{N_A a^3}\left(-\frac{n_{CuR}(t)}{\frac{P_{Au}}{P_{Cu}}(n_{Cu} - n_{CuR}(t)) + n_{CuR}(t)} + \frac{n_{Cu} - n_{CuR}(t)}{n_{Au} - \frac{P_{Au}}{P_{Cu}}(n_{Cu} - n_{CuR}(t)) + n_{Cu} - n_{CuR}(t)}\right), \tag{13}$$

$$\dot{n}_{AuR}(t) = \frac{4P_{Au}}{N_A a^3}\left(\frac{n_{Au} - n_{AuR}(t)}{n_{Au} - n_{AuR}(t) + \frac{P_{Cu}}{P_{Au}}n_{AuR}(t)} - \frac{n_{AuR}(t)}{n_{AuR}(t) - \frac{P_{Cu}}{P_{AuR}}n_{AuR}(t) + n_{Cu}}\right). \tag{14}$$

The full analytical solutions to Eqs. (13) and (14) can be found in the Supplemental Material [16]. Approximations to the transcendental solutions, where negligibly contributing terms are eliminated, are

$$t = \frac{-N_A a^3}{4P_{Cu}\left(\frac{P_{Au}}{P_{Cu}}n_{Cu} + n_{Au}\right)^3}\left[C_1 + C_2 n_{CuR}(t) + C_3 \ln\left(\left(\frac{P_{Au}}{P_{Cu}n_{Au}} + \frac{1}{n_{Cu}}\right)n_{CuR}(t) - \frac{P_{Au}n_{Cu}}{P_{Cu}n_{Au}}\right)\right] \tag{15}$$

and

$$t = \frac{-N_A a^3}{4P_{Cu}\left(\frac{P_{Au}}{P_{Cu}}n_{Cu} + n_{Au}\right)^3}\left[C_1 + C_2\left(n_{Cu} - \frac{P_{Cu}}{P_{Au}}n_{AuR}(t)\right) + C_3 \ln\left(\left(\frac{P_{Au}}{P_{Cu}n_{Au}} + \frac{1}{n_{Cu}}\right)\left(n_{Cu} - \frac{P_{Cu}}{P_{Au}}n_{AuR}(t)\right) - \frac{P_{Au}n_{Cu}}{P_{Cu}n_{Au}}\right)\right], \tag{16}$$

where the constants are

$$C_1 = n_{Au}^2 n_{Cu}\left(n_{Au}\left(\frac{P_{Au}}{P_{Cu}} - 1\right) - \frac{n_{Cu}}{2}\right), \tag{17}$$

$$C_2 = \left(\frac{P_{Au}}{P_{Cu}} - 1\right)\left(\frac{P_{Au}}{P_{Cu}}n_{Cu} + n_{Au}\right)\left(\frac{P_{Au}^2}{P_{Cu}^2}n_{Cu}^2 + \frac{P_{Au}}{P_{Cu}}n_{Cu}n_{Au} - n_{Au}(n_{Cu} + n_{Au})\right), \tag{18}$$

and

$$C_3 = \frac{P_{Au}}{P_{Cu}}n_{Cu}n_{Au}(n_{Cu} + n_{Au})^2. \tag{19}$$

P_{Cu} and P_{Au} can be determined at a given temperature by fitting experimental XPS depth profile data for the molar concentration of Au and Cu on the right side of the interface. Specifically, to determine the permeabilities of Cu and Au at 460 K, the molar concentrations of Cu and Au were calculated from the four XPS depth profiles after annealing times of 0, 20, 60, and 240 min at each Cu wedge thickness. Calculation details are described in Secs. 2, 4, and 5 of the Supplemental Material [16,24–26,49–51]. The best-fit values for the permeabilities were $P_{Cu} = 13.8 \times 10^{-13}$ m/s and $P_{Au} = 6.7 \times 10^{-13}$ m/s. These were optimized by minimizing the sum squared error between the full analytical solutions for the atomic percentage on the right side of the Au-Cu interface, [Eqs. (7) and (8) combined with Eqs. S10 and S11] and XPS-derived molar areal concentration values [16].

A plot of the time-dependent interdiffusion behavior, for a 49-nm Au layer on a 10-nm Cu layer and the permeabilities determined at 460 K, is shown in Fig. 5. Both the approximate solution of Eq. (15) and the full solution of Eq. S10 [16] are shown, with good agreement. The time dependent behavior of G is also shown in Fig. 5, where G is calculated using the DMM described in the next section. For this particular system, within 250 min at 460 K, a majority of the interdiffusion has occurred and a major decrease in G is evident.

B. Thermal Interface Conductance Modeling

The DMM is used to predict G at large temperatures relative to the Debye temperature of either interfaced material

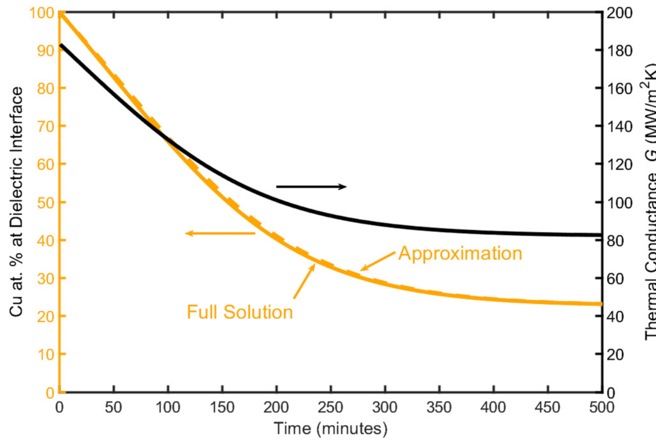

FIG. 5. Time dependent at. % Cu on right, according to Fig. 4 schematic, and *G* calculated using the DMM (described in the next section). The majority of interdiffusion and *G* decrease occurs within the first 250 min of annealing at 460 K for a 49-nm Au film deposited on a 10-nm Cu film.

[2,52–54]. To model the Au_xCu_{1-x}-Al_2O_3 thermal interface conductance, the DMM described in Freedman *et al.* was employed. For the alloy, Freedman *et al.* used a Born-Von Karman phonon dispersion that continuously varied based on alloy composition defined by Vegard's law and the average atomic mass. This was paired with the experimentally measured phonon dispersion of Al_2O_3 [7]. Following the approach of Jeong *et al.* for calculating *G* for adhesion layers, we treat phonon wavelengths smaller than the thickness of the adhesion layer as being transmitted from the adhesion layer to the dielectric, and larger wavelengths as being transmitted from the Au layer directly into the Al_2O_3 [2].

In order to make comparative predictions with experimental data, the analytical interdiffusion model was utilized to calculate the alloy composition of the two metal layers as a function of annealing time and temperature (P_{Au} and P_{Cu} are temperature dependent), for the as-deposited Cu thicknesses (0–10 nm) and Au thickness of interest (49 nm). The alloy compositions of each layer were then input into the DMM model. The DMM predicted values of *G* for the Au-Cu film as-deposited, after annealing at 460 K, and for the fully intermixed film after annealing at 520 K are shown in Fig. 6, with

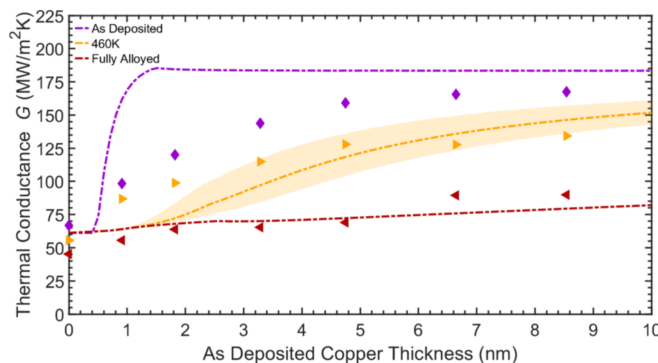

FIG. 6. DMM predictions of *G* compared with experimental values for 49 nm of Au. The shaded region depict a 30% error in both permeabilities.

experimental data for comparison. For the 460-K DMM, the permeabilities used were $P_{Cu} = 13.8 \times 10^{-13}$ m/s and $P_{Au} = 6.7 \times 10^{-13}$ m/s, and an interdiffusion time of 60 min. One hour was used because the sample was first annealed at 360 K for 30 min, 440 K for 30 min, and then 460 K for 30 min; the XPS data in Fig. 2 shows that little interdiffusion had occurred at 360 K, and the permeabilities were assumed to be similar at 440 and 460 K. The shaded regions of the DMM demarcate a 30% error in the permeabilities, for both the P_{Cu} and P_{Au}.

Although the DMM does not consider the quality of the interface, and so is a very rudimentary model for the prediction of *G*, the reasonable agreement with data shown in Fig. 6 indicate that it can be useful to estimate thermal interface conductance for various interdiffusion conditions [55,56].

IV. CONCLUSION

We present systematic measurements of metal overlayer and metal adhesion layer interdiffusion through the use of our XPS depth profiling measurements, and report the corresponding evolution of *G* as a function of heat treatment temperature and Cu-adhesion layer thickness. Using our experimental depth profiling results we have derived an analytical model to describe the unique interdiffusion behavior in the thin film Au-Cu system. Utilizing this model for DMM calculations, we have created a method for electronic/thermal engineers to simulate interdiffusion in Au-Cu films, and roughly predict its impact on *G* with a dielectric substrate, according to the thermal conditions of their devices and the initial film thicknesses. The methodology we present opens the door for future studies with different film thicknesses and other material combinations where the major resistance to interdiffusion is at the interface between metal films. Such experiments would provide permeability values to use in the model for the prediction of the evolution of *G* due to high temperature exposure.

ACKNOWLEDGMENTS

The authors thank Prof. G. Rohrer of the Materials Science and Engineering Department of Carnegie Mellon for helpful discussion and his review of this work. We also acknowledge support provided by the National Science Foundation (NSF CBET 1403447), the Data Storage Systems Center (DSSC) at Carnegie Mellon University, and Northrop Grumman through the University Research Program.

APPENDIX: EXPERIMENTAL METHODOLOGY DETAILS

1. Preparation of layered Cu/Au sample

Two layered samples of Cu and Au were prepared by evaporative deposition from Cu and Au e-beam sources onto a 14 × 14 mm, 2-mm thick, Mo substrate (Valley Design Corp.) and one 14 × 14 mm, 1 mm-thick, polished Al_2O_3 *c*-plane (0001) dielectric substrate using a rotating shadow mask deposition tool [57]. The shadow mask is located between the substrate and Cu e-beam source, which produces spatially varying flux gradients, and deposits a wedge shape with a linear thickness gradient across the substrate. A Mo substrate was used because it is a conductive material required for

XPS measurements. Neither Cu nor Au will interdiffuse with Mo at an elevated temperature [58–60]. The Al_2O_3 wafer was selected for the dielectric substrate in thermal interface conductance measurements in order to make direct comparisons to literature reported measurements of interface conductance [2,7]. The substrates were cleaned with isopropanol and dried in air. The Cu wedge thin film was deposited at a rate of 0.2 nm/min under ultrahigh vacuum (UHV), at a base pressure of 2×10^{-9} Torr and a temperature of 300 K. Next, a uniform thickness of Au film was deposited at a rate of 0.2 nm/min under UHV on top of the Cu wedge and a temperature of 300 K.

2. EDX thickness characterization

After deposition, the sample was transferred to a Tescan scanning electron microscope with an Oxford Instruments X-max 80-mm^2 detector for EDX characterization. The thicknesses of Au and Cu layers were mapped at 36 points on a 10×10 mm area grid with 2-mm spacing centered on the Mo substrate. The thicknesses of the Au and Cu layers were mapped at 169 points on a 12×12 mm area grid, with 1-mm spacing centered on the Al_2O_3 substrate. The EDX spectra (0–10 keV) were collected by rastering a high voltage electron beam (20 keV) across a $50 \times 50\,\mu$m area. The obtained spectra were used to quantify the thickness (<100 nm) of Cu and Au with the INCA ThinFilmID software. We assume that the Cu adhesion layer is sandwiched between the Au layer and the Mo/Al_2O_3 substrate, since the characterization depth of the electron beam is larger than 300 nm [61].

3. XPS depth profiling characterization

XPS depth profiling is a destructive technique that repeatedly measures local composition and removes material from the surface through ion sputtering. The local through-plane composition was measured at each sputtering depth with a characterization depth of $\sim$1 nm. XPS depth profiles of layered Au-Cu samples were conducted at four selected Cu thicknesses characterized by EDX in a ThetaProbe surface analysis system (ThermoFisher Scientific Inc.). XPS depth profiles were obtained from the as-deposited bilayer films and at the same thicknesses after annealing at temperatures of 320, 360, 440, and 520 K for 30 min each. Al K_α radiation from a monochromatic x-ray source (1486.6 eV) was focused onto a 50-μm diam beam spot. The x-ray photoelectron spectra were collected at binding energies with 10 eV ranges around the Cu $2p_{3/2}$, Au $4f_{7/2}$, and Mo $3p_{3/2}$d peaks, which were used for quantifying the through-plane composition. The scanned area was sputtered across an area of 1 mm^2 by rastering a focused Ar^+ beam (3 keV) with a backfilled pressure of 1×10^{-5} Torr between XPS measurements. These scans were gathered at an analyzer pass energy of 100 eV with a 0.01 eV step size. The peak area of XP spectra were determined by performing the Thermo "Smart" background subtraction and peak fitting with a fixed 30% Lorentzian and Gaussian line shape in the Thermo Advantage Processing software. The relative atomic composition was calculated by applying Thermo sensitivity factors to adjust the peak areas.

4. Thermal interface conductance measurements

Measurements of G were made with the noncontact optical pump/probe method FDTR [62,63]. In FDTR, a 488-nm continuous wave pump beam has its intensity modulated by an electro-optic modulator at a given frequency and is focused onto the surface of the sample. The modulated beam periodically heats the surface of the sample, and the temperature of the sample, in turn, oscillates at the same frequency but with a phase lag related to the sample's thermal interface conductance. A coincident 532-nm continuous wave probe beam is reflected by the sample surface, and its intensity is modulated by the change in reflectivity, caused by the periodically changing temperature (i.e., thermoreflectance). The reflected modulated pump and probe beams are individually collected by a photodiode and the phase lag of temperature with respect to heat flux is determined by a lock-in amplifier. The phase lag between pump and probe is measured as a function of modulation frequency (at 30 logarithmically spaced frequencies between 100 kHz and 5 MHz). We fitted the solution to the heat diffusion equation for layered systems to this phase lag versus frequency data, where the only unknown parameter in the solution is G [64].

While in some cases our films were thinner than the optical penetration depth of our pump and probe lasers [65], the data did not require special analysis because of the modulation frequencies used and the high thermal conductivity of the metal bilayer, in accordance with Fig. 4 of the work done by Schmidt *et al.* [66]. Any light that did transmit through the metal bilayer did not contribute to the thermoreflectance signal due to Al_2O_3's transparency. The possibility of needing special analysis for oxidation of the Cu by the oxide substrate was eliminated because the Gibbs free energy of formation of Cu_2O is higher than that of Al_2O_3 [67].

5. High Temperature Annealing

After using a micromanipulator to have FDTR scan across the sample and measure G as a function of Cu thickness, the sample was annealed in an UHV environment with a base pressure of 2×10^{-8} Torr. The sample was then rescanned with FDTR. By iterating between vacuum annealing and measuring thermal interface conductance, G was determined as a function of initial Cu thickness and annealing temperature. The annealing temperatures for this sample were 360, 440, 460, 480, and 520 K with an annealing time of 30 min per anneal.

TABLE I. FDTR measurement uncertainty

Parameter	Percent uncertainty
Laser spot size	±5%
Metal thermal conductivity [68]	±5%
Metal volumetric heat capacity	±6%
Metal thickness	±10%
Al_2O_3 thermal conductivity	±2%
Al_2O_3 volumetric heat capacity	±2%

6. Conductance Uncertainty Analysis

The uncertainty of the values reported in Fig. 3 result from uncertainty in the input parameters for the fitting analysis of G.

Table I lists the uncertainty in the input fitting parameters. The uncertainty propagation involves fitting for G, as each parameter is varied positively and negatively by the listed uncertainty. The value of the error bars in Fig. 3 are calculated by taking the residual sum of squares, using the fitted thermal conductances for each parameter with the uncertainty listed in Table I in comparison to the fitted conductance from the nominal value [53].

[1] A. L. Moore and L. Shi, Mater. Today **17**, 163 (2014).
[2] M. Jeong, J. P. Freedman, H. J. Liang, C.-M. Chow, V. M. Sokalski, J. A. Bain, and J. A. Malen, Phys. Rev. Appl. **5**, 014009 (2016).
[3] A. Majumdar and P. Reddy, Appl. Phys. Lett. **84**, 4768 (2004).
[4] S. Sadasivam, U. V. Waghmare, and T. S. Fisher, J. Appl. Phys. **117**, 134502 (2015).
[5] D. G. Cahill, P. V. Braun, G. Chen, D. R. Clarke, S. Fan, K. E. Goodson, P. Keblinski, W. P. King, G. D. Mahan, A. Majumdar, H. J. Maris, S. R. Phillpot, E. Pop, and L. Shi, Appl. Phys. Rev. **1**, 011305 (2014).
[6] T. S. English, J. C. Duda, J. L. Smoyer, D. A. Jordan, P. M. Norris, and L. V. Zhigilei, Phys. Rev. B **85**, 035438 (2012).
[7] J. P. Freedman, X. Yu, R. F. Davis, A. J. Gellman, and J. A. Malen, Phys. Rev. B **93**, 035309 (2016).
[8] B. C. Gundrum, D. G. Cahill, and R. S. Averback, Phys. Rev. B **72**, 245426 (2005).
[9] D. H. Olson, K. M. Freedy, S. J. McDonnell, and P. E. Hopkins, Appl. Phys. Lett. **112**, 171602 (2018).
[10] P. E. Hopkins, P. M. Norris, R. J. Stevens, T. E. Beechem, and S. Graham, J. Heat Trans. **130**, 062402 (2008).
[11] J. W. Elmer, T. A. Palmer, and E. D. Specht, J. Vac. Sci. Technol. A **24**, 978 (2006).
[12] A. N. Aleshin, V. K. Egorov, B. S. Bokstein, and P V Kurkin, Thin Solid Films **223**, 51 (1993).
[13] R. Ravi and A. Paul, J. Mater. Sci. Mater. Electron. **23**, 2152 (2012).
[14] M. R. Pinnel, Gold Bull. **12**, 62 (1979).
[15] T. Surholt, Y. M. Mishin, and C. Herzig, Phys. Rev. B **50**, 3577 (1994).
[16] See Supplemental Material at http://link.aps.org/supplemental/10.1103/PhysRevB.99.115418 for more data and modeling information supplemental to the main paper, which includes Refs. [24–26,49–51,68].
[17] B. Navinšek, P. Panjan, A. Žabkar, and J. Fine, Nucl. Inst. Methods Phys. Res. B **2**, 670 (1984).
[18] K. Wittmaack, Vacuum **34**, 119 (1984).
[19] S. Hofmann and A. Zalar, Thin Solid Films **60**, 201 (1979).
[20] S. Hofmann, Y. Liu, W. Jian, H. L. Kang, and J. Y. Wang, Surf. Interface Anal. **48**, 1354 (2016).
[21] K. Wittmaack, *Practical Surface Analysis: Ion and Neutral Spectroscopy*, Vol. 2 (Wiley, New York, 1992), p. 105.
[22] K. Wittmaack, J. Appl. Phys. **53**, 4817 (1982).
[23] J. W. Coburn and E. Kay, CRC Crit. Rev. Solid State Sci. **4**, 561 (1973).
[24] S. Hofmann, Y. S. Han, and J. Y. Wang, Appl. Surf. Sci. **410**, 354 (2017).
[25] R. Payling, M. Aeberhard, J. Michler, C. Authier, P. Chapon, T. Nelis, and L. Pitchford, Surf. Interface Anal. **35**, 334 (2003).
[26] H. Shimizu, M. Ono, and K. Nakayama, Surf. Sci. **36**, 817 (1973).
[27] J. DuMond and J. P. Youtz, J. Appl. Phys. **11**, 357 (1940).
[28] P. M. Hall, J. M. Morabito, and N. T. Panousis, 41, 341 (1977).
[29] J. C. M. Hwang and R. W. Balluffi, J. Appl. Phys. **50**, 1339 (1979).
[30] M. E. Glicksman, *Diffusion in Solids: Field Theory, Solid State Principles, and Applications* (Wiley, New York, 2000).
[31] H. Mehrer, *Diffusion in Solids: Fundamentals, Methods, Materials, Diffusion-Controlled Processes* (Springer Science & Business Media, Berlin, 2007).
[32] I. Kaur, Y. Mishin, and W. Gust, *Fundamentals of Grain and Interphase Boundary Diffusion* (Wiley, New York, 1995).
[33] P. Shewmon, *Diffusion in Solids* (Springer, Berlin, 2016).
[34] J. C. Fisher, J. Appl. Phys. **22**, 74 (1951).
[35] R. T. P. Whipple, Dublin Philos. Mag. J. Sci. **45**, 1225 (1954).
[36] T. Suzuoka, J. Japan Inst. Metals **2**, 176 (1961).
[37] J. M. Poate, P. A. Turner, W. J. Debonte, and J. Yahalom, J. Appl. Phys. **46**, 4275 (1975).
[38] W. J. DeBonte, J. M. Poate, C. M. Melliar-Smith, and R. A. Levesque, J. Appl. Phys. **46**, 4284 (1975).
[39] W. Preis and W. Sitte, J. Appl. Phys. **79**, 2986 (1996).
[40] W. M. Paulson and J. E. Hilliard, J. Appl. Phys. **48**, 2117 (1977).
[41] H. E. Cook and J. E. Hilliard, J. Appl. Phys. **40**, 2191 (1969).
[42] G. H. Gilmer and H. H. Farrell, J. Appl. Phys. **47**, 3792 (1976).
[43] G. H. Gilmer and H. H. Farrell, J. Appl. Phys. **47**, 4373 (1976).
[44] D. Gupta and P. S. Ho, Thin Solid Films **72**, 399 (1980).
[45] L. G. Harrison, Trans. Faraday Soc. **57**, 1191 (1961).
[46] J. M. Poate, K. Tu, and J. W. Mayer, in *Thin Films-Interdiffusion and Reactions* (Wiley, New York, 1978), pp. 161–195.
[47] J. C.-M. Hwang, *On the Measurement of Grain Boundary Diffusion at Low Temperatures* (Cornell University Press, Ithaca, NY, 1978).
[48] J. C. M. Hwang, J. D. Pan, and R. W. Balluffi, J. Appl. Phys. **50**, 1349 (1979).
[49] Sputtering Yields for Argon, http://www.npl.co.uk/science-technology/surface-and-nanoanalysis/services/sputter-yield-values (2014).
[50] S. Hofmann and J. Y. Wang, J. Surf. Anal. **9**, 306 (2002).
[51] Y. Liu, W. Jian, J. Y. Wang, S. Hofmann, and K. Shimizu, Appl. Surf. Sci. **331**, 140 (2015).
[52] R. J. Stevens, P. M. Norris, and L. V Zhigilei, *Proceedings of 2004 ASME International Mechanical Engineering Congress and Exposition*, IMECE2004-60334 (ASME, 2004), p. 37.
[53] Y. Hu, L. Zeng, A. J. Minnich, M. S. Dresselhaus, and G. Chen, Nat. Nanotechnol. **10**, 701 (2015).
[54] R. J. Stevens, A. N. Smith, and P. M. Norris, J. Heat Transfer **127**, 315 (2005).
[55] R. J. Stoner and H. J. Maris, Phys. Rev. B **48**, 16373 (1993).
[56] E. T. Swartz and R. O. Pohl, Rev. Mod. Phys. **61**, 605 (1989).
[57] B. Fleutot, J. B. Miller, and A. J. Gellman, J. Vac. Sci. Technol. A **30**, 061511 (2012).

[58] D. Priyadarshini, P. Kondratyuk, Y. N. Picard, B. D. Morreale, A. J. Gellman, and J. B. Miller, J. Phys. Chem. C **115**, 10155 (2011).

[59] M. A. Payne, J. B. Miller, and A. J. Gellman, Corros. Sci. **91**, 46 (2015).

[60] J. W. He, D. W. Goodman, D. G. Naugle, and D. L. Cocke, Mater. Lett. **10**, 250 (1990).

[61] J. C. Russ, in *Fundamentals of Energy Dispersive X-Ray Analysis* (Butterworth-Heinemann, Oxford, 1984), pp. 17–41.

[62] J. A. Malen, K. Baheti, T. Tong, Y. Zhao, J. A. Hudgings, and A. Majumdar, J. Heat Trans. **133**, 081601 (2011).

[63] A. J. Schmidt, R. Cheaito, and M. Chiesa, Rev. Sci. Instrum. **80**, 094901 (2009).

[64] D. G. Cahill, Rev. Sci. Instrum. **75**, 5119 (2004).

[65] L. G. Schulz, J. Opt. Soc. Am. **44**, 357 (1954).

[66] J. Yang, E. Ziade, and A. J. Schmidt, J. Appl. Phys. **119**, 95107 (2016).

[67] N. Birks, G. H. Meier, and F. S. Pettit, *Introduction to the High Temperature Oxidation of Metals* (Cambridge University Press, Cambridge, 2006).

[68] C. Y. Ho, M. W. Ackerman, K. Y. Wu, T. N. Havill, R. H. Bogaard, R. A. Matula, S. G. Oh, and H. M. James, J. Phys. Chem. Ref. Data **12**, 183 (1983).